Front. Earth Sci. 2021, 15(4): 831–848
https://doi.org/10.1007/s11707-021-0927-4

RESEARCH ARTICLE

Evolution of pore structure in organic shale with type III kerogen and high kaolinite content in Ningwu Basin

Qiang XU[1], Hangbing LIN (✉)[2], Yue ZHAO[1], Bo WANG[3], Bin MA[4], Rong DING[5], Jianxin WANG[6], Tao HOU[7]

1 General Prospecting Institute, China National Administration of Coal Geology, Beijing 100039, China
2 Purdue University Northwest, Hammond IN 46323, USA
3 Information Institute of the Ministry of Emergency Management of China, Beijing 100029, China
4 Shanxi Lanhua CBM Co. Ltd, Jincheng 048026, China
5 PetroChina Coalbed Methane Co. Ltd, Beijing 100028, China
6 Research Institute of China National Offshore Oil Corporation, Beijing 100028, China
7 PetroChina Huabei Oilfield Company, Renqiu 062550, China

Abstract Special deposition environment makes organic-rich shales in Ningwu Basin have type III kerogen and high kaolinite content, which are also famous as the kaolinite ore. The specific composition of shale in Ningwu Basin can change the pore structure and thus, influence the shale gas storage and transport. This study focuses on the pore structure and its evolution in shales with type III kerogen and high kaolinite content. In this study, 14 Upper Paleozoic shale samples, whose total organic matter contents (TOC) range from 0.39% to 5.91% and maturities (represented by vitrinite reflectance) range from 1.22% to 2.06%, were collected. Scanning electron microscopy (SEM), high-pressure mercury injection, and low-temperature N_2 adsorption experiments were used to analyze pore structure of these shale samples. Results show that when the TOC content is smaller than 1.4%, the kaolinite content decreases linearly and quartz content increases linearly with increasing the TOC content. In contrast, when TOC content is $> 1.4\%$, the clay content tends to increase with increasing TOC. Based on the SEM images, organic pores and clay pores were identified in shale samples with type III kerogen and high kaolinite content. During the maturation process, the kaolinite content decreases and illite content increases with increasing the vitrinite reflectance. At the same time, the pore volume and pore surface area both increase with increasing the vitrinite reflectance, and it may be because more organic pores and clay pores in the illite were generated during the maturation process. This study can provide further understandings of shale gas accumulation in shale with type III kerogen and high kaolinite content.

Received February 25, 2021; accepted June 21, 2021

E-mails: 454123526@qq.com; hangbinglin@gmail.com

Keywords pore structure, type III kerogen, kaolinite, low-temperature N_2 adsorption, high-pressure mercury porosimetry, influencing factors

1 Introduction

In recent years, shale gas production increases rapidly in China and USA, and have become an important natural gas resource (Curtis, 2002; Wang et al., 2014a; Chen et al., 2020). In China, shale gas production is mainly from shales with type I kerogen, such as Longmaxi Formation and Qiongzhusi Formation in Sichuan basin (Li et al., 2016a, 2019a; Feng et al., 2018; Guo, 2019; Liu et al., 2021). Although numerous shale gas was found in the shales with type III kerogen in China, such as Qinshui Basin and Ordos Basin, breakthroughs in shale gas production have not occurred in these shales by now (Li et al., 2016b; Zhang et al., 2019; Kuang et al., 2020). More efforts need to be performed to study the shale gas in shales with type III kerogen. Shale gas is mainly stored in the pores of shale and pores are also the tunnels for shale gas transport. Shale reservoirs contain numerous microscale pores and fractures, and the pore and fracture systems together control the storage and migration of shale gas (Sanyal et al., 2006; Yang et al., 2016a; Xiong et al., 2017; Bahadur et al., 2018). In recent years, research on micro- to nanoscale pores in shale has received increasing attention. The pore structure of shale reservoirs have become important indicators for effective shale gas exploration and development (Yang et al., 2016b; Hazra et al., 2018; Zhang et al., 2018; Wang et al., 2019; Zhou et al., 2020).

Extensive researches have been carried out on the pore types, pore size distribution and pore evolution in organic-

rich shale (Wang et al., 2014b, 2018; Liu et al., 2016; Li et al., 2016c; Li et al., 2017, 2020). It was found that the pore structure is controlled by the mineral composition, organic matter type, abundance, maturity, and burial depth (Wang et al., 2014b, 2018; Liu et al., 2016; Li et al., 2016b; Li et al., 2017, 2020). In addition, the deposition environment obviously causes the difference in mineral composition, total organic carbon (TOC) content and kerogen type (Li et al., 2019b). Compared to marine shale, the shales deposited in transitional and terrestrial environments have higher clay content and lower quartz content (Yang et al., 2016c). In addition, the kerogen in shales formed in the transitional facies is usually type III (Wang et al., 2020).

The organic shale in Ningwu Basin was formed in specific deposition environment, and there are high contents of kaolinite in the organic shale. The special composition would change the pore structure of the organic shale and affect the shale gas storage and transport (Sun et al., 2017; Zhang et al., 2021). In this study, it is focused on the pore structure and its controlling factors of shale with type III kerogen and high kaolinite. Shale samples from the Ningwu Basin were studied by scanning electron microscopy (SEM), N_2 adsorption, and mercury intrusion experiments The evolution of pore structure with increase the maturity is also analyzed.

2 Geological setting

The Ningwu Basin (Fig. 1) belongs to the Shanxi Block, which is in the middle transition zone of the North China Plate. During the Paleozoic period, the Ningwu Basin is under north–south-oriented tectonic stress. As a result of the subduction of the Kura–Pacific Plate, the tectonic compression stress direction has changed from north–south to east–west. Since the Cenozoic, the tectonic stress has transformed into an east–west extensional stress.

In the Late Paleozoic, the North China Plate gradually regressed, forming multiple sets of marine-continental transitional facies and black shale, represented by the Upper Carboniferous and Lower Permian. Upper Carboniferous black shale was formed in the low-level marsh environment of coastal and shallow delta plains under the background of regression, and the Lower Permian black shale was formed in the continental river and delta sedimentary environment. The lithology of the Upper Paleozoic black shale in the Ningwu Basin is mainly carbonaceous mud shale, silty mud shale, and black mud shale. Shale is widely distributed throughout the basin characterized by large thickness, high organic carbon content, and high maturity. It is a potential stratum for the exploration of shale gas. The shale in the Ningwu Basin has mainly undergone five structural control transformations of the late Hercynian movement, the Indosinian movement, the early-mid Yanshanian movement, the late Yanshanian movement, and the Himalayan movement. In the late Hercynian movement, the shale depth continued to increase. The heating temperature and evolution degree of shale organic matter slowly increase, and R_o value rises to 0.6%–1.3%. In the late Indosinian period, shale was uplifted, and the thermal evolution of organic matter basically stopped at this stage. In the early to middle period of Yanshan Movement, the burial depth of shale further increased after the Middle Jurassic sedimentation, and the R_o value of organic matter further increased. In the late Yanshan Movement, the Ningwu Basin formed a large-scale syncline structure due to strong compression. During the Himalayan period, the shale in the study area continued to rise. Until the late Himalayan movement, the formation was basically stable or slightly subsided. The organic matter evolution of shale at this stage will not be further developed.

3 Samples and methods

Pore characteristics are influenced by different factors, such as organic matter, clay minerals, quartz, maturation process, and so on (Fig. 2) (Li et al., 2017, 2020). In this study, a total of 14 Carboniferous-Permian shale samples from four wells in the Ningwu Basin were collected. Samples H1, S1, S4, X3, N3 are Shangxi formation, and samples H2, H3, S2, S5, X2, N2 are Taiyuan Formation. Samples S3, X1 N1 are Benxi Formation (Table 1). The shale samples of Taiyuan Formation and Benxi Formation are mainly formed in the lagoon microface and more affected by the sea water. Shale samples of Shanxi Formation are mainly formed in the delta microfacies. From Benxi Formation to Shanxi Formation, the sea level keeps falling and there are multiple cycles during this period. The organic carbon content, vitrinite reflectance (R_o), and microscopic composition were tested. In addition, X-ray diffraction (XRD), N_2 adsorption, mercury intrusion porosimetry (MIP), and Scanning Electron Microscope (SEM) analyses were carried out to obtained the mineral composition and pore structure of the shale samples. The organic carbon content was tested by using a CS-230 infrared carbon and sulfur analyzer. The test was carried out according to standard GB/T 19145-2003 "Determination of Total Organic Carbon in Sedimentary Rocks." For this test, a 5–10 g sample was ground to 60 mesh. The vitrinite reflectance was tested using a Leica DM4500p polarizing microscope and DFC450C full-spectrum microscopy photometer. The test was based on standard SY/T 5124-1995 "Method for the determination of vitrinite reflectance in sedimentary rocks".

Besides, the XRD was used to analyze the mineralogical characteristics of shale. All rock samples were ground to a particle size below 40 μm and analyzed using a Rigaku SmartLab X-ray diffractometer. The analyses were based on standard SY/T 5163-2010 "Clay minerals and common

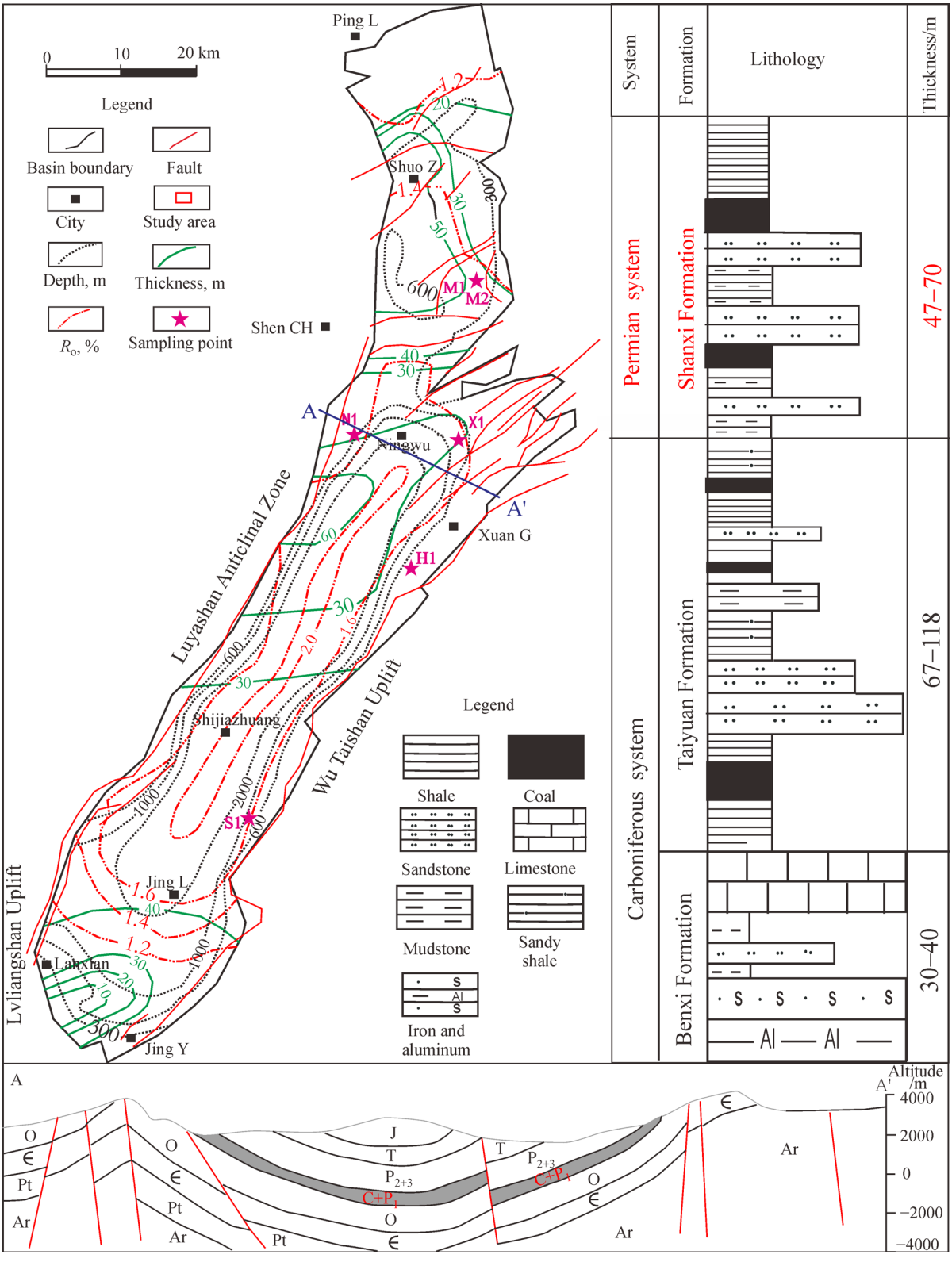

Fig. 1 Schematic map showing sampling wells location (Xu et al., 2018).

non-ferrous metals in sedimentary rocks". Low-temperature nitrogen adsorption tests were performed with a Gold Ångström spectrum V-Sorb 2800TP specific surface area and pore size analyzer. The tests were based on standard GB/T 21650.3-2011. For the high-pressure mercury intrusion test, a QUANTACHROME POREMASTER

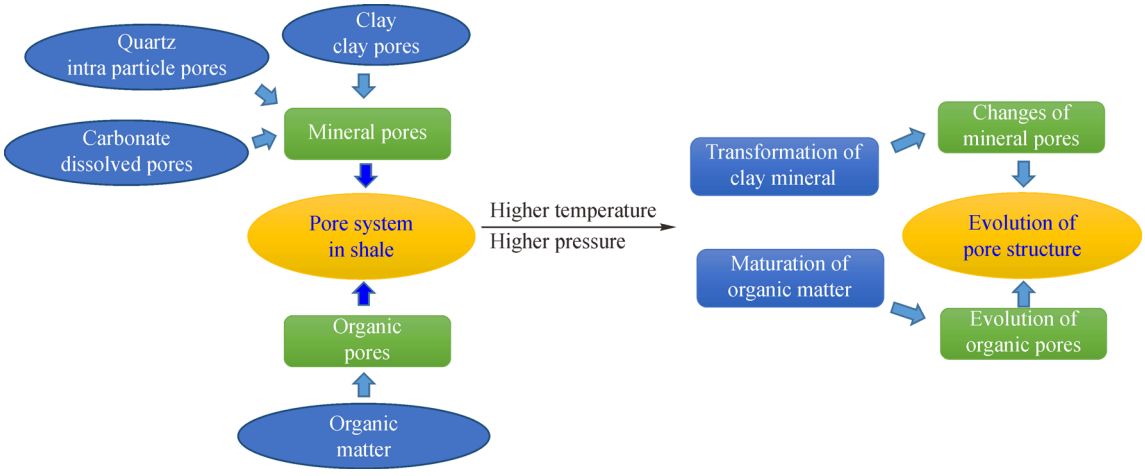

Fig. 2 The influencing factors on pore structure (Li et al., 2017, 2020).

automatic mercury intrusion measurement was used according to standard GB/T 21650.1-2008. All testing experiments were completed at the Shanxi Coal Bed Methane Testing and Research Institute. The maceral composition was tested based on the Chinese standard SY/T 6414-2014 "Maceral identification and statistical methods on polished surfaces of whole rocks."

The complexity and heterogeneity of the shale pore structure can be quantitatively described by using the fractal dimension (D), which generally ranges from 2 to 3 (Avnir and Jaroniec, 1989; Kanniah et al., 2012). Smaller fractal dimension is small means that the pores are uniform and have smooth surfaces. Several methods have been proposed for the calculation of the fractal dimension based on N_2 adsorption isotherms. The Frenkel–Halsey–Hill (FHH) model is considered to be the most effective method and has been widely used for various porous materials (Zhou et al., 2020). Based on the FHH model, the fractal dimension can be obtained based on the nitrogen adsorption data by using the following equation:

$$\ln V = (\mathrm{D}-3)\ln[\ln(p_0/p)] + B, \quad (1)$$

where V represents the volume of adsorbed gas molecules at equilibrium pressure p in cm^3/g; D is the fractal dimension; p_0 is the saturated vapor pressure in MPa; and B is a constant.

4 Results

4.1 Composition of the shale samples

Table 1 shows the mineral composition of the Carboniferous–Permian shales in the Ningwu Basin. The mineral composition of the shale samples was quantitatively determined by XRD. Based on the results, the clay mineral content is the highest, followed by quartz. In the shale samples, the clay mineral content is 43.70%–90.00%, with an average of 69.42%. These clay minerals are mainly composed by kaolinite, ranging from 51.3% to 97.6%, followed by illite with 2.4% to 44.3% and montmorillonite with 0.0% to 6.3%. The content of brittle minerals, such as quartz, is 10.00%–50.60%, with an average of 29.64%. There are also small amount of feldspar, calcite, and pyrite (Table 1). The TOC content ranges from 0.39% to 5.91%, with an average of 2.22%. The maturity of organic matter (R_o) varies from 1.22%–2.21%, with an average of 1.66%, which means the organic matter is stayed in high mature to over mature stages. It can be seen that the R_o value of some shale samples is larger than that of the shale sample with larger depth from the same drilling. This may be because the hydrological and mineral characteristics, as hydrology would affect the reservoir temperature and some minerals can catalyze the evolution of organic matter. It should be also noted that by now it is still a big problem to obtain the accurate R_o value as most of organic particles in shale are too small.

4.2 Pore types based on SEM

The micro- to nanoscale pores in shales can be divided into three types: organic pores, inorganic pores, and micro-fractures (Slatt and O'Brien, 2011; Loucks et al., 2012). Based on the SEM observing, the Carboniferous-Permian shale of the study area contains many nano-organic organic pores (Fig. 3). These organic pores are in elliptical, polygonal, and irregular shapes with clear boundaries and widely varying size (10 nm–50 μm; Figs. 3(a)–3(e)). The morphology of the organic pores is related to the organic matter carrier. SEM images show that OM is commonly mixed with clay minerals (Figs. 3(a), 3(c), and 3(d)). There are also some slit-type pores in the organic matter. These slit pores are mainly formed by tectonic stress, and thus the original organic matter pores collapse (Figs. 3(a)–3(c)). In

Table 1 Mineral compositions and characteristic parameters of shale samples

Sample ID	Depth/m	Formation	TOC/%	R_o/%	Mineraloglcal composition/%						Clay composition/%		
					Quartz	Feldspar	Clay	Dolomite	Calcite	Pyrite	I	K	C
H1	933.2	Shanxi	3.17	1.67	21.8		76.9	0	0	1.3	17	83	0
H2	1045.1	Taiyuan	2.01	1.22	30.2		69.0			0.8	14.4	85.6	0
H3	1090.1	Taiyuan	1.05	1.27	42.8		56.3			0.9	26.4	73.6	
S1	1228.1	Shanxi	5.8	1.61	12.9		82.0		5.1		2.4	97.6	0
S2	1303.1	Taiyuan	1.34	2.21	47.8		52.2				13.8	86.2	0
S3	1360.1	Benxi	0.93	1.37	32		67.1		0.9		29.4	67.8	2.8
S4	1241	Shanxi	2.08		15.9	20.4	63.7				11.7	88.3	0
S5	1287	Taiyuan	1.45		21.9	6.6	49.2	3.4	5.7		44.3	51.3	4.4
X1	1238.1	Benxi	1.39	1.69	50.6		43.7	5.7			44.3	51.3	4.4
X2	1169.1	Taiyuan	5.91	1.82	22.4		71.6			6	5.5	94.5	0
X3	1082.1	Shanxi	0.39	1.67	10		90.0				5.9	94.1	0
N1	911.1	Benxi	0.62	2.06	29.3		68.5			2.2	7.6	86.1	6.3
N2	860	Taiyuan	2.51	1.63	28.8		67.4			3.8	17	83	0
N3	770.6	Shanxi	2.44	1.68	21.5		77.8			0.7	9.4	90.6	0

Notes: I: illite, K: kaolinite, C: chlorite

some organic matter, there are few pores or no pores (Fig. 3(e)), indicating that the development of organic pores is controlled by multiple factors.

Many inorganic pores were also found in the Carboniferous-Permian shale in Ningwu Basin (Figs. 3(a)–3(i)). As the kaolinite content in the shale sample is very high, large number of kaolinite pores can be seen by the SEM observing as shown in Figs. 4(a) and 4(b). These kaolinite pores are in slit-like shapes and can easily form a pore-seam network system (Figs. 4(a) and 4(b)). The connectivity of these pores is good, which effectively increases the shale reservoir storage space and is also the main channel for gas transport.

Inter-particle pores represent the space remaining after the deposition and compaction of primary pores between mineral particles or crystals. Inter-particle pores usually have triangular, rectangular, and irregular shapes. The pore morphology is affected by the morphology and mutual contact relationship of the mineral particles. The sizes of these pores vary widely from 80 nm–2 μm (Figs. 4(c), 4(d), 4(e), 4(f), 4(g), and 4(h)). In addition, the sizes of inter-particle pores are related to the mineral particle size and the degree of compaction. In contrast, intra-particle pores are less developed in the study area (Fig. 4(i)); they are mainly distributed in mineral particles such as quartz and calcite.

Figure 4(i) are the dissolution pores, which many be formed by acidic fluids generated during the thermal evolution of shale. Dissolution pores are rare in the shale samples in the study area. Their morphology is irregular, and the size varies from 80 to 900 nm (Fig. 4(i)). Dissolution pores are formed by minerals that partially or completely dissolved. Thus, the size and morphology of the remaining dissolution pores is the determined by the dissolved particles. The microfractures of the shale in the study area can be divided structural and nonstructural microfractures based on their mode of formation. SEM observing also shows that structural microfractures are linear with a short extension and width ranges from 100 nm to 2 μm (Figs. 4(d) and 4(g)).

4.3 Results of high-pressure mercury injection experiment

Mercury intrusion experiments is one of the most effective methods for the analysis of the pore in shale (Clarkson et al., 2013; Li et al., 2018; Liu et al., 2019; Qin et al., 2020). Mercury intrusion experiment can be used to determine the porosity, pore size distribution (PSD), and pore connectivity. With increasing pressure, mercury is first injected into large sized microfractures and then into nanoscale pores. The mercury injection curves of these organic shales in Ningwu Basin are shown in Fig. 5. These mercury intrusion curves can be divided into two types. The first type is represented by samples S2, S4, and S5, showing a three-stage distribution. The initial mercury injection pressure is 1 psi and the mercury saturation slowly increases with increasing the injection pressure. When the pressure increases from 20 psi to 2000 psi, there is almost no increase in mercury saturation. When pressure is larger than 2000 psi, the mercury saturation increase rapidly with increasing pressure.

The second type shows a two-stage curve. With the mercury injection pressure ranging from 1 to 10 psi, mercury saturation increase to 80%. When the pressure is larger than 10 psi, the mercury saturation almost shows no

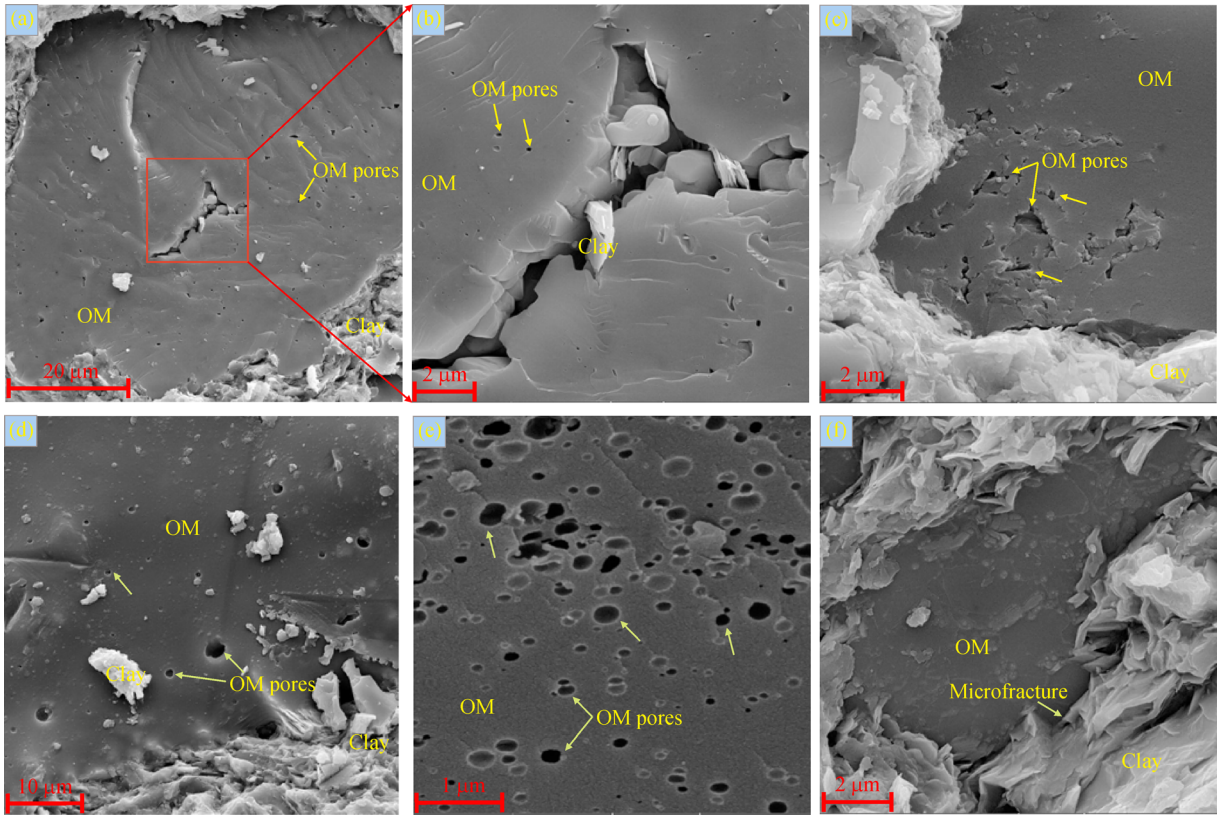

Fig. 3 Organic pores in SEM images. (a) and (b) different shapes of OM pores, well S301, 1214 m; (c) slit OM pores, well S301, 1214 m; (d) circular and elliptical OM pores, well H201, 1117 m; (e) densely distributed circular organic pores, S301,1214 m; (f) organic matter without pore, well N901, 829 m.

changes, indicating these are fewer pores at this pressure stage as illustrated in PSD diagram in Fig. 5. The mercury injection curve shows that a complex pore network developed in the shale in this area. The different types of mercury injection curves of these shale samples can be caused by the organic matter and inorganic matter. The shale sample S2 have the highest R_o, and during the maturation process, more small nanopores were generated. Thus, at the high pressure stage, the mercury saturation increases significantly. The samples S4 and S5 have larger feldspar content and lower quartz content than other shale samples. This makes their fewer macropore in shale sample S4 and S5, and makes the mercury injection curves belong to the first type.

The pore size distribution based on the mercury intrusion experiment is shown in Fig. 6. As show in Fig. 6, the pores size distribution shows a multimodal distribution. Peaks appear at size of 6–11 nm and 10 μm. The pore structure characteristics are listed in Table 2. The total specific surface area (TSSA) ranges from 0.0004 to 1.4690 m^2/g, with an average of 0.3942 m^2/g. The TSSAs of S1 and S2 samples are larger than other samples, reaching 3.7167–5.7247 m^2/g. The total pore volume (TPV) of all the shale samples ranges from 0.002 to 0.0223 cm^3/g, with an average of 0.1755 cm^3/g. The total surface area and total volume obtained the mercury intrusion experiment are smaller than those determined in the liquid nitrogen adsorption test. The porosity of shale sample obtained in the mercury injection experiment ranges from 0.52% to 5.58%, with an average of 3.15% as shown in Table 2.

4.4 Results of low-temperature N_2 adsorption experiment

Figure 7 shows the low-temperature nitrogen absorption and desorption curves of shale samples. Based on the IUPAC classification, the shale adsorption curves are mainly H3 and H4, and the hysteresis loops of the shale experimental data mainly belong to type II based on the classification of Brunauer et al. (1940), indicating pores in Ningwu Basin are parallel plate-shaped, slit-shaped, cylindrical, and mixed-type pores with various shapes. In the low-pressure stage ($0 < p/p_0 < 0.4$), the adsorption isotherm slightly increases with increasing the pressure. The adsorption at this stage is the single-layer adsorption on the shale surface or filling the micropores. When the relative pressure increases from 0.45 to 0.9, adsorption amount increases steadily and slowly, indicating that the

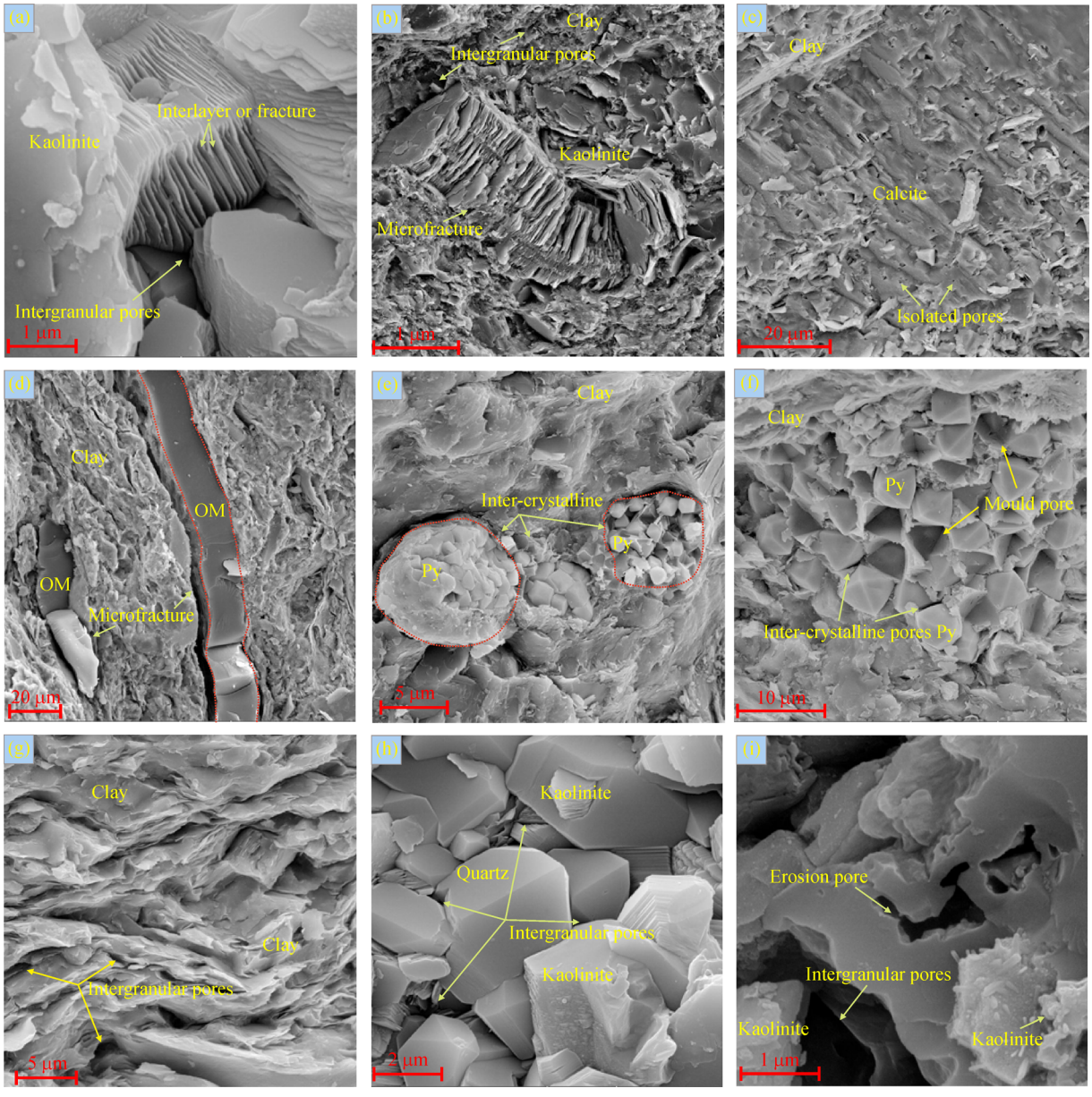

Fig. 4 The inorganic pores and micro-fractures in the shale samples. (a) Kaolinite pores, well H201, 938 m; (b) kaolinite pores, N901, 829 m; (c) intra-particle pores, well N901, 829 m; (d) micro-fractures and inter-particle pores between organic matter and clay minerals, well H201, 914 m; (e) inter-particle pores in pyrite, well S301, 1214 m; (f) pores formed by pyrite, well S301, 1332m; (g) pores in clay minerals, well X702, 1078 m; (h) inter-particle pores, well H201, 938 m; (i) dissolution pores, well H201, 1049 m.

single-layer adsorption transformed to multilayer adsorption. When the relative pressure is larger 0.9, the adsorption amount increase sharply due to capillary condensation in the mesopores and macropores. In addition, although the adsorption amount increases rapidly at this stage, the adsorption amount does not reach saturation, indicating the existence of macropores. Because of capillary aggregation, the desorption and adsorption curves do not completely overlap, resulting in a hysteresis loop. The desorption curves of several samples abruptly drop at a relative pressure (p/p_0) of 0.5 and this phenomena were also found in previous studies on shale. Based on morphology of the hysteresis loop, closed ink-bottle pores are well developed on one side of these samples. As shown in Fig. 7, as the TOC content of the sample increases, the N_2 adsorption amount and hysteresis ring area increase, indicating there are larger number of ink-bottle-like pores in the organic matter of shale samples.

The pore volume, specific surface area, and average pore diameter can be used to quantify the pore structure

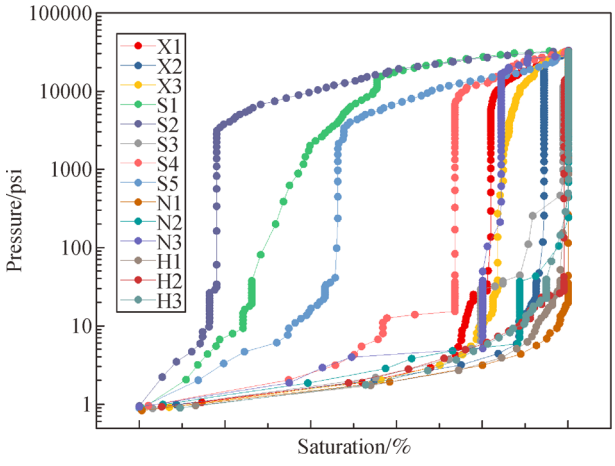

Fig. 5 The mercury saturation under different mercury intrusion pressure.

parameters of shale samples. These pore structure parameters of shale obtained by N_2 adsorption were shown in Table 3 and Fig. 8. Based on the IUPAC classification method, the pores in the porous media can be divided into three categories according to the pore size, that is, micropores ($D < 2$ nm), mesopores (2–50 nm), and macropores ($D > 50$ nm). As shown in Table 3, the TSSA of each sample ranges from 5.8391 to 18.2043 m^2/g, with an average of 11.6065 m^2/g. The micropore specific surface area varies from 0.0001 to 4.0997 m^2/g, with an average of 1.2840 m^2/g, and the mesopore specific surface area ranges from 4.9164 to 14.9122 m^2/g, with an average of 10.1807 m^2/g, accounting for the largest proportion of the mesopore specific surface area. The macropore specific surface area ranges from 0.0707 to 0.2556 m^2/g, with an average of 0.1572 m^2/g (Fig. 8(a)). The porosity ranges from 3.25% to 7.49%, with an average of 4.87%. The results show that the TSSA of shale is mainly controlled by micropores and mesopores, accounting for more than 90% of the TSSA. The TPV of each sample ranges from 0.0122 to 0.0310 cm^3/g, with an average of 0.2738 cm^3/g. The TPV is mainly controlled by mesopores and macropores, which account for more than 90%. Among this, mesopores account for more than 80% of the TPV (Fig. 8(b)).

The pore size distributions obtained by low pressure N_2 adsorption experiment of shale samples is shown in Figs. 9(a) and 9(b). From Fig. 9(a), it can be seen that the incremental surface area gets the largest value at width range of 2–3 nm. There are also small peaks in the pore width range of 15–30 nm (Fig. 9(a)). Samples S4 and S5 have a higher specific surface area than other samples. High-SSA pores are conducive to gas adsorption and occurrence. However, they will complicate gas desorption and diffusion. The TPV of each sample is mainly controlled by mesopores with pore diameters ranging from 10 to 50 nm and macropores with diameters of 50–300 nm (Fig. 9(b)). The contribution of macropores to the TPV of each sample considerably differs, which reflects the complexity of the shale macropore structure in this area.

4.4.1 Fractal dimension characteristics of pores based on N_2 adsorption

The fractal dimensions D_1 and D_2 were calculated based on the adsorption data at p/p_0 = 0–0.45 and p/p_0 = 0.45–1.00, respectively as N_2 adsorption isotherms show different behavior. In the relative pressure range of p/p_0 = 0–0.45, the adsorption of N_2 molecules mainly occurs on the surface of the monolayer. Therefore, the fractal dimension of the shale surface represented by D_1 reflects the

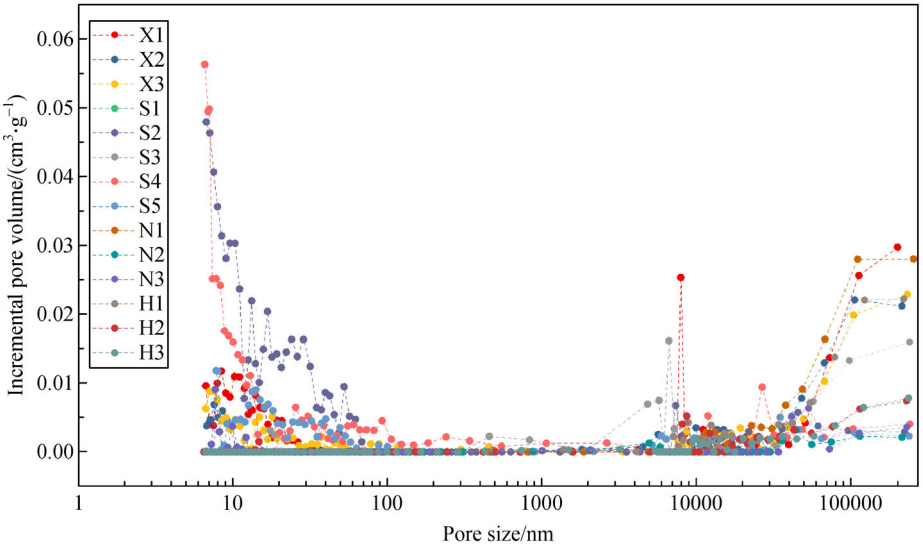

Fig. 6 Pore size distribution with the mercury intrusion method.

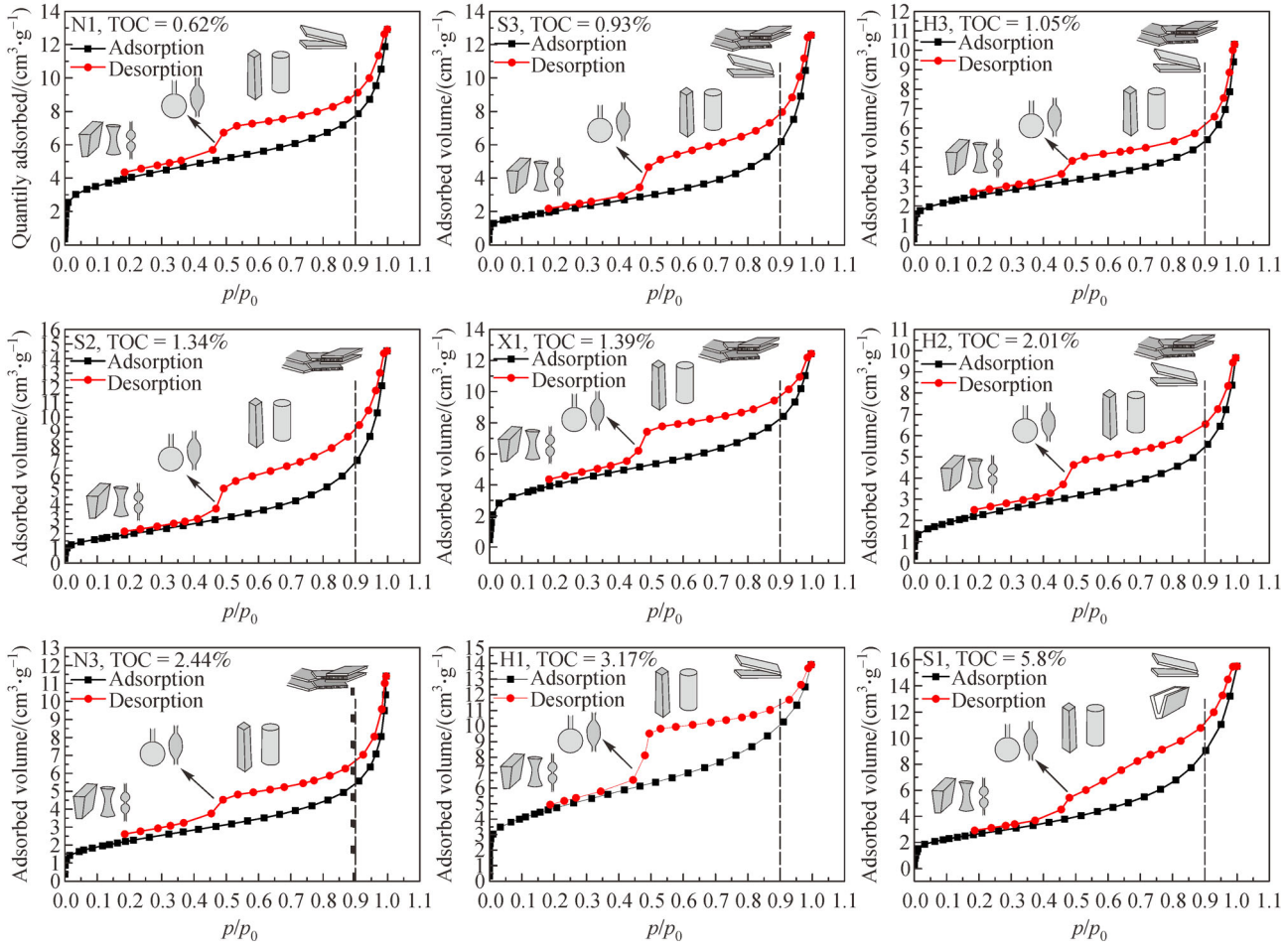

Fig. 7 Representative N_2 adsorption/desorption isotherms and the corresponding pore shapes of different samples.

Table 2 Pore structure parameters of shale obtained by MIP

Sample ID	TSSA/($m^2 \cdot g^{-1}$)	TPV/($cm^3 \cdot g^{-1}$)	Porosity/%
H1	0.0024	0.0161	4.00
H2	0.0142	0.0057	1.29
H3	0.0012	0.0059	1.54
S1	3.7167	0.0162	4.21
S2	5.7247	0.0209	5.06
S3	0.0453	0.0133	3.14
S4	0.5797	0.0060	1.54
S5	0.9435	0.0076	2.26
X1	1.4690	0.0223	5.58
X2	0.4629	0.0166	4.38
X3	0.9469	0.0187	4.58
N1	0.0091	0.0206	5.03
N2	0.0004	0.0020	0.52
N3	0.2552	0.0036	0.93

roughness of the pore surface. In the relative pressure range of p/p_0 = 0.45–1.00, single-layer adsorption transforms to multilayer adsorption and pore-filling adsorption, and the N_2 molecules exhibit capillary condensation characteristics. Therefore, D_2 represents the fractal dimension of the pore structure, which can be used to characterize the irregularity of the pore structure (Pan et al., 2018; Yuan and Rezaee, 2019).

Based on the FHH model and the linear relationship between $\ln V$ and $\ln(\ln(p_0/p))$, the fractal dimension can be obtained from the slope of the fitted curve. The calculated fractal dimensions are shown in Table 4 and Fig. 10. The value of D_1 ranges from 2.062 to 2.310, with an average of 2.215, and the value of D_2 ranges from 2.668 to 2.828, with an average of 2.756. Based on the curves between $\ln V$ and $\ln(\ln(p_0/p))$, the average correlation coefficient is 0.8993, indicating that all shale pore structures have strong fractal characteristics. In all the shale samples, D_1 is smaller than D_2, indicating that the heterogeneity of smaller mesopores is weaker than that of larger mesopores. The analysis

Table 3 Pore structure parameters of shale obtained by N_2

Smple ID	TSSA/ ($m^2 \cdot g^{-1}$)	SSA_{mic}/ ($m^2 \cdot g^{-1}$)	SSA_{mes}/ ($m^2 \cdot g^{-1}$)	SSA_{mac}/ ($m^2 \cdot g^{-1}$)	TPV/ ($cm^3 \cdot g^{-1}$)	PV_{mic}/ ($cm^3 \cdot g^{-1}$)	PV_{mes}/ ($cm^3 \cdot g^{-1}$)	PV_{mac}/ ($cm^3 \cdot g^{-1}$)	R_{ave}/ nm	Porosity/ %
H1	18.2043	3.208	14.9122	0.0841	0.0211	0.0013	0.0176	0.0022	7.33	5.15
H2	8.4958	0.5006	7.9093	0.0859	0.0146	0.0002	0.0121	0.0023	9.61	3.25
H3	9.004	2.0091	6.7894	0.2019	0.0148	0.0008	0.0084	0.0056	11.22	3.76
S1	13.9538	0.4185	13.3018	0.2335	0.0252	0.0001	0.0212	0.0039	11.14	6.38
S2	12.2099	0.0001	11.9925	0.2173	0.024	0.0000	0.0193	0.0047	12.60	5.75
S3	10.0063	0.0001	10.0259	0.2003	0.0201	0.0000	0.0159	0.0042	12.34	4.69
S4	13.9672	0.8566	12.8705	0.2401	0.031	0.0003	0.0258	0.0049	11.41	7.49
S5	13.9538	0.4185	13.4646	0.0707	0.0252	0.0001	0.0234	0.0017	11.14	7.14
X1	14.0239	2.7524	11.1585	0.113	0.0180	0.0011	0.0143	0.0026	8.07	4.55
X2	6.8867	0.5387	6.2381	0.1099	0.0122	0.0002	0.0095	0.0025	9.72	3.25
X3	13.9796	1.9287	11.9641	0.0868	0.0192	0.0008	0.0159	0.0025	9.13	4.70
N1	13.4832	4.0997	9.3081	0.0754	0.0175	0.003	0.0145	0.0027	9.26	4.31
N2	5.8391	0.6671	4.9164	0.2556	0.0141	0.0002	0.0079	0.006	13.03	3.50
N3	8.4837	0.5784	7.6787	0.2266	0.0168	0.0002	0.011	0.0056	11.70	4.25

Notes: TSSA is the total specific surface area, m^2/g; TPV is the total pore volume, cm^3/g; R_{ave} is average pore size, nm; SSA_{mic}, SSA_{mes} and SSA_{mac} are the specific surface area of micro-, meso- and macropores, respectively; PV_{mic}, PV_{mes} and PV_{mac} are the pore volume of micro-, meso- and macropores, respectively.

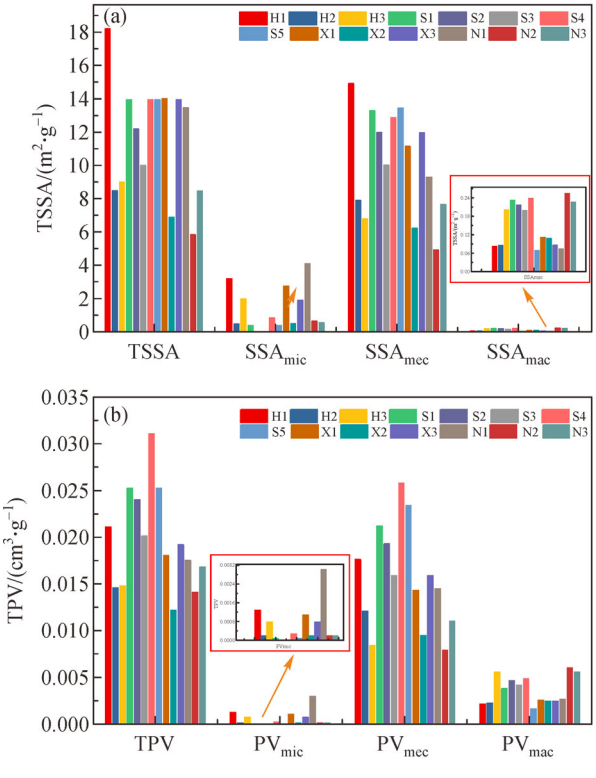

Fig. 8 pore volume and surface area distribution of the shale samples.

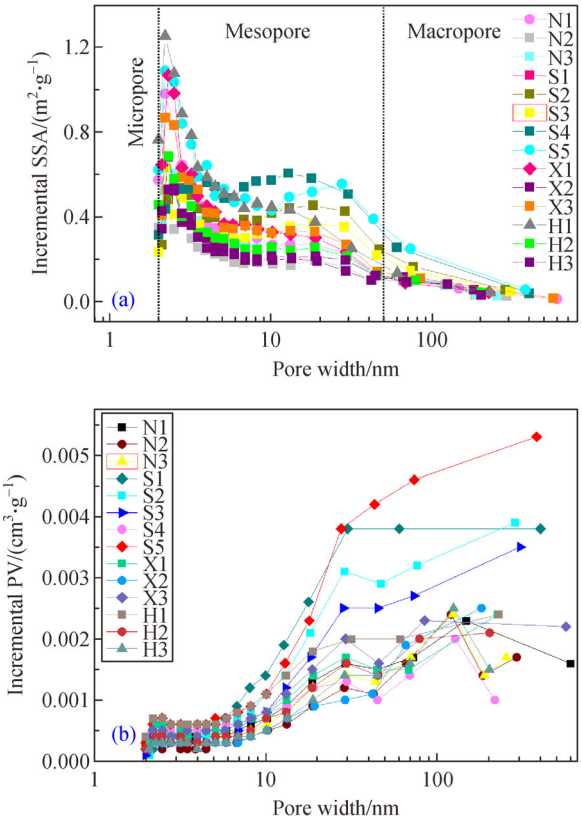

Fig. 9 Pore size distribution of different shale samples: (a) incremental SSA vs. pore width, (b) incremental PV vs. pore width.

shows that D_2 of each test sample is positively correlated with the TSSA and negatively correlated with the average pore diameter. This is consistent with the results of previous studies (Zhou et al., 2016; Pan et al., 2018) and this also indicates that D_2 is more suitable for the

Table 4 Fractal analysis of the samples from N_2 adsorption

Samples	D_1	R_1^2	D_2	R_2^2
H1	2.207	0.7749	2.828	0.9388
H2	2.271	0.8714	2.747	0.9858
H3	2.300	0.8057	2.746	0.9998
S1	2.087	0.8497	2.726	0.8917
S2	2.279	0.8943	2.668	0.9571
S3	2.309	0.8767	2.726	0.9574
X1	2.062	0.8286	2.809	0.9669
N1	2.112	0.7531	2.828	0.9649
N3	2.310	0.8716	2.726	0.9999

characterization of the pore structure characteristics (Fig. 11). The parameter D_1 is negatively correlated with the TSSA and positively correlated with the average pore diameter, which is contrary to previous results (Yang et al., 2014; Jiang et al., 2016). This also reflects the strong heterogeneity of nanopores in this area.

5 Discussion

5.1 The relationship between organic matter and clay minerals

In shale, the organic matter can be deposited with clay minerals as the clay minerals have strong adsorption capacity. Figure 12 shows the relationship between clay content, quartz content and organic matter content. It can be seen that with TOC content increasing from 0% to 1.4%, the clay content decreases linearly. However, when TOC content increase from 1.4% to 6.0%, the clay content exhibits increasing continually In contrast, the correlation between quartz content and organic matter content is opposite to that between clay content and organic matter content. With TOC increasing from 0% to 1.4%, the quartz increase linearly and with TOC increasing 1.4% to 6.0%, the quartz content decreases continually. In this study, it is considered that the relationship between clay content, quartz content and organic matter content is complex and

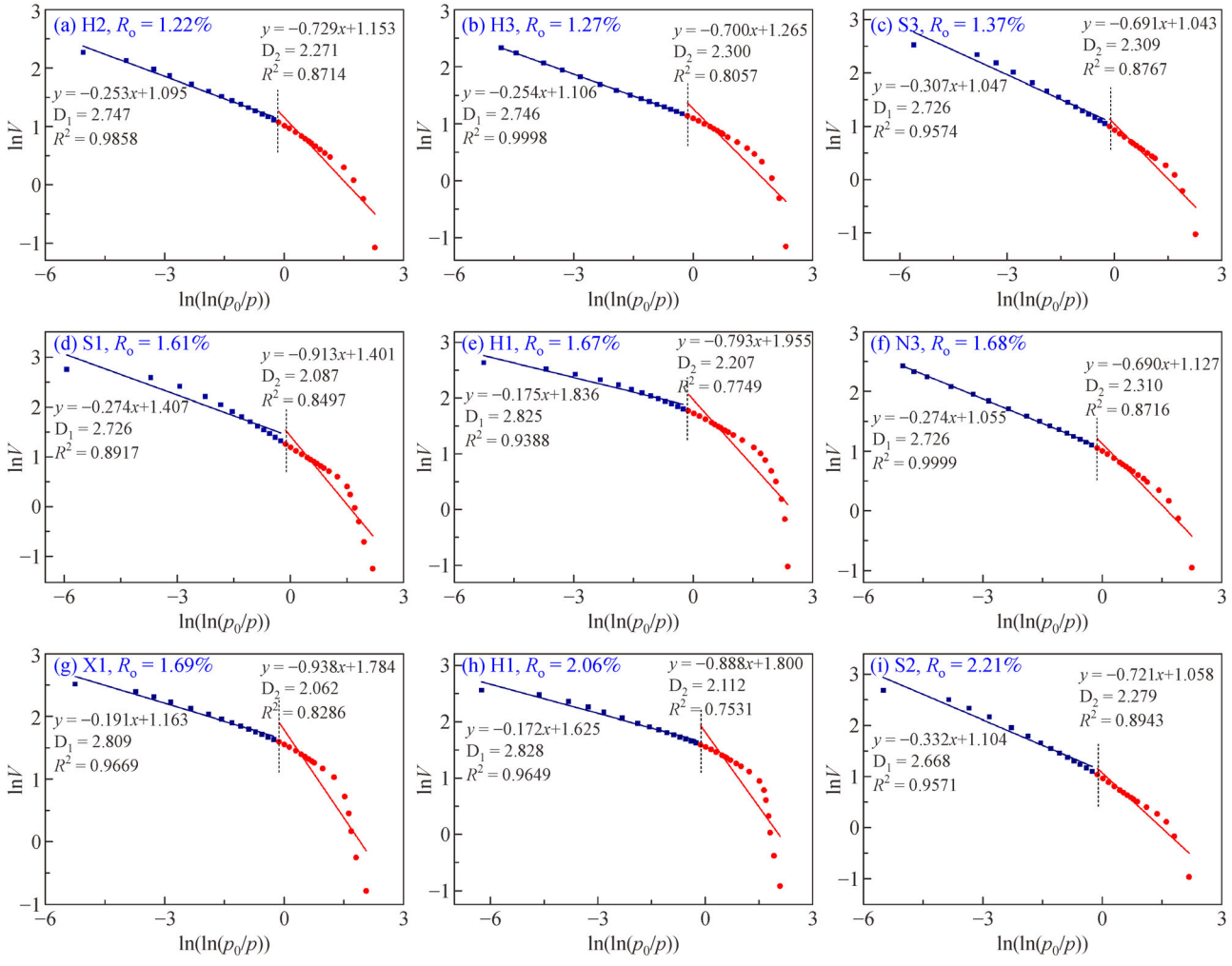

Fig. 10 Plots of ln$V$ vs ln(ln(p_0/p)) from N_2 adsorption data.

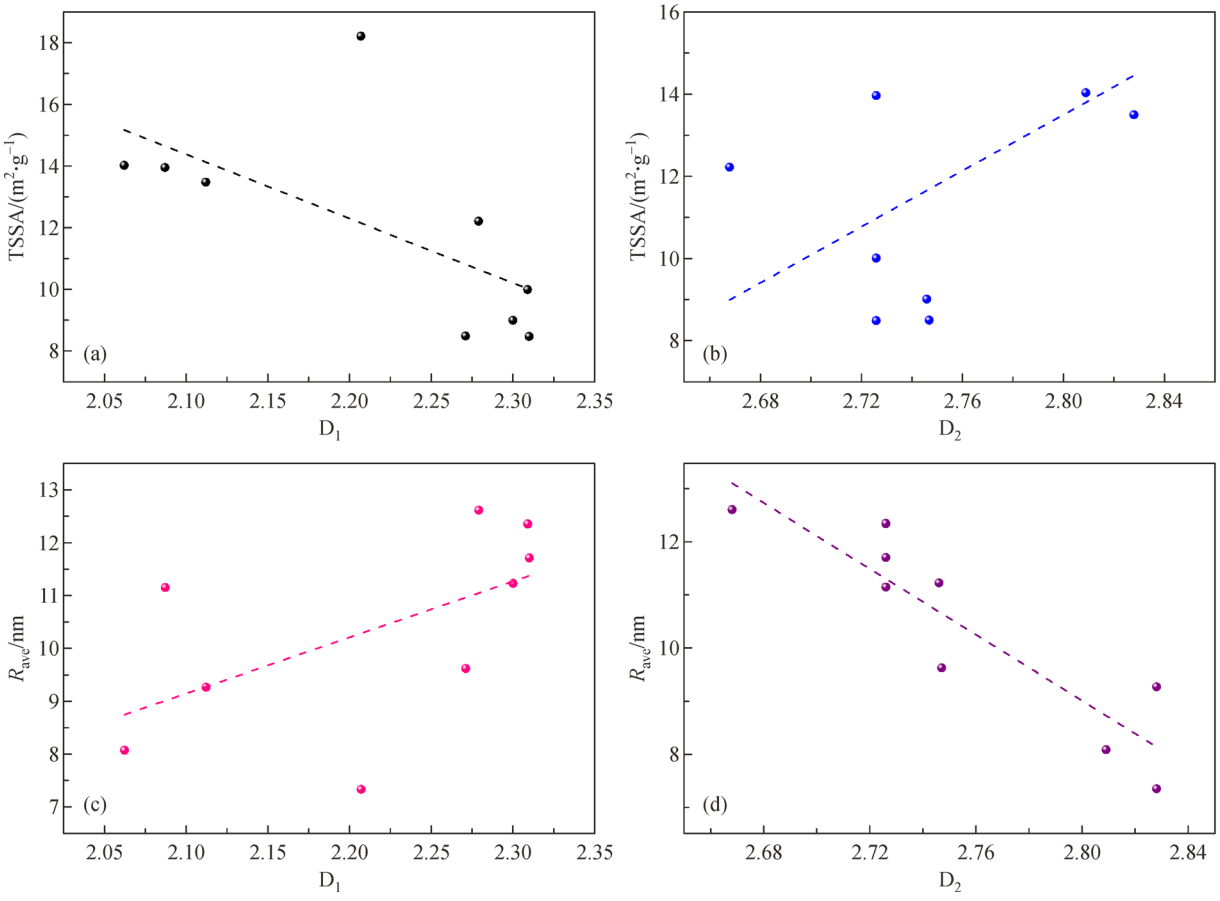

Fig. 11 Correlation between fractal dimensions and pore structure parameters.

the relationship is determined by the deposition environment and deposition process. When the organic matter content is quite low ($<1.4\%$), the organic matter is not deposited along with the clay minerals. On the contrary, the deposition of quartz and the performance of organic matter are closely related. When the TOC content is higher than 1.4%, the deposition of organic matter, clay mineral and quartz particle changes. It is obvious that the organic matter content and clay content are positively correlated, and this is may be that the organic matter is deposited along with the clay minerals due to the adsorption of the clay minerals. It should be also noted that the current organic matter content is different from that in the deposition process as some atoms of organic matter were released during the maturation process. The R_o value of the shale sample in this study ranges from 1.22% to 2.21%. The shale sample with higher R_o value would have higher incremental TOC content during the TOC recovery process. The shale with $R_o > 2.0\%$ were marked in Fig. 12.

During the geological process, the organic matter evolves as affected by the temperature and time. The molecular structure and pores structure of organic matter changes, and the petroleum and natural gas are generated. Besides, the clay minerals also evolve with the changing of

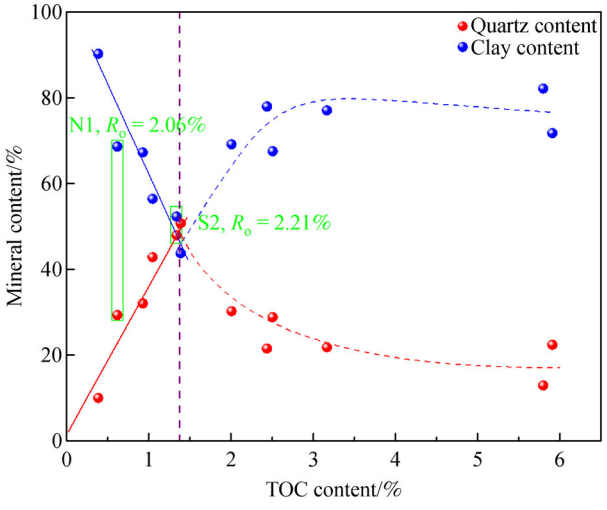

Fig. 12 The relationship between clay content, quartz content and organic matter content.

pressure, temperature and underground fluids. It can be seen that in general, with the vitrinite reflectance increasing, the kaolinite content decreases and the illite content

increase. This is mainly because that with pressure and temperature increasing, the kaolinites change to the illite, and this would also affect the pore structure of the shale samples. Also, from Fig. 13, it can be seen there are two correlation curves between kaolinite content and vitrinite reflectance. It may be because the fluid environment is different. Based on Fig. 13, we can also found the kaolinite content in the shale samples is always is higher than illite content.

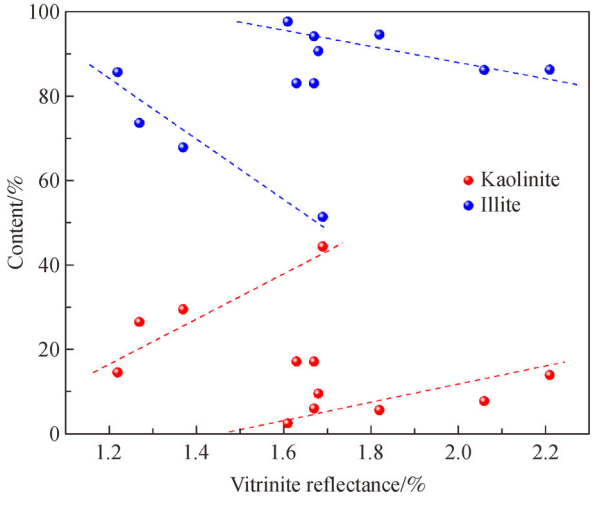

Fig. 13 the relationship between kaolinite content, illite content and vitrinite reflectance.

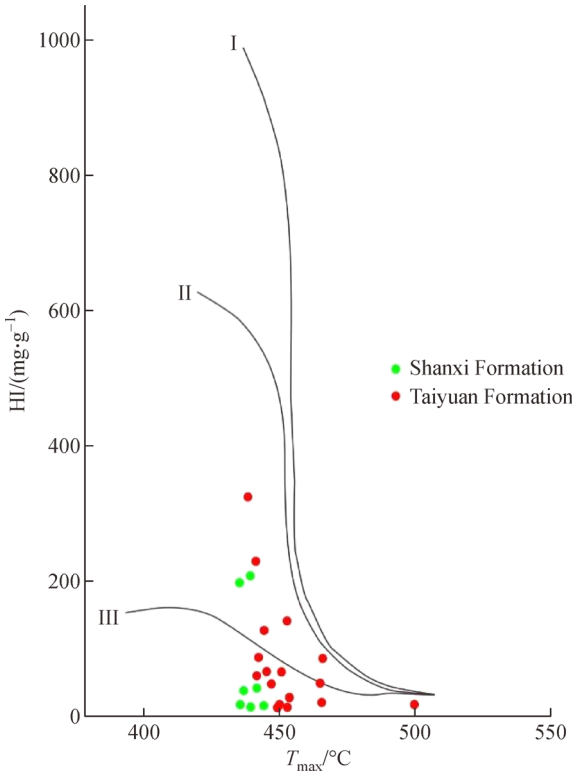

Fig. 14 The relationship between HI and T_{max} of Carboniferous-Permian shale in the study area.

5.2 The effect of organic matter on pore structure

The pore structure of shale reservoirs is controlled by multiple factors such as depositional environment, structural movement and lithological composition (Clarkson et al., 2013; Xu et al., 2017; Zhang et al., 2018). In this study, the main factors controlling the development of microscale pores in the Upper Paleozoic shale in the Ningwu Basin were analyzed based on the organic geochemical characteristics and mineral characteristics. Organic matter is the key factor to affect the pore structure in shale, and there are many organic pores in the shale samples as observed by the SEM experiment.

The Carboniferous–Permian shale in the study area is in the high- to overmaturity stage (average R_o = 1.22%–2.21%). Kerogen is mainly composed of vitrinite, with a mass fraction of 80%–95%, followed by chitin. The kerogen type of the shale samples mainly belonging to type III kerogen, and there are also a small amount of type II kerogen in the shale samples (Fig. 14). Compared with type I and type II kerogen, type III kerogen has fewer organic nanopores (Jarvie et al., 2007), and the specific surface area and volume of the pores are smaller.

Organic pores are an important part of the shale pore system (Shi et al., 2015; Yang et al., 2016c). The SEM images show that organic pores are one of the main types of pores in shale in this area. Organic pores are generally mesopores and micropores with sizes below 200 nm (Katz and Arango, 2018). A higher TOC is the basis for the formation of many organic pores. Compared with HPMP, N_2 adsorption can be used to measure pores with sizes below 200 nm more precisely. Therefore, the TPV, TSSA, and porosity values determined with N_2 adsorption are all greater than those measured by HPMP (Fig. 9). The TOC content of continental shale in this area ranges from 0.39%–5.91%, with an average of 1.61%. The TOC value of individual samples (such as S1 and X2) reaches as high as 5.8% (Table 1). The TOC is positively correlated with the porosity measured by N_2 adsorption (Fig. 15(a)), indicating that the organic carbon content of shale promotes nanoscale development. However, the correlation between the porosity of the HPMP test and TOC cannot be observed, which may be related to the larger pore size range of the HPMP test. The TOC weakly correlates with the TPV and TSSA of shale (Figs. 15(b) and 15(c)). This observation contradicts with previous results (Curtis et al., 2012; Fu et al., 2015; Liu et al., 2015), indicating that organic matter pores in this area are mainly isolated pores and the organic matter content plays a minor role in controlling the pore structure. When the TOC content of shale increases, micro- to nanoscale pores will be

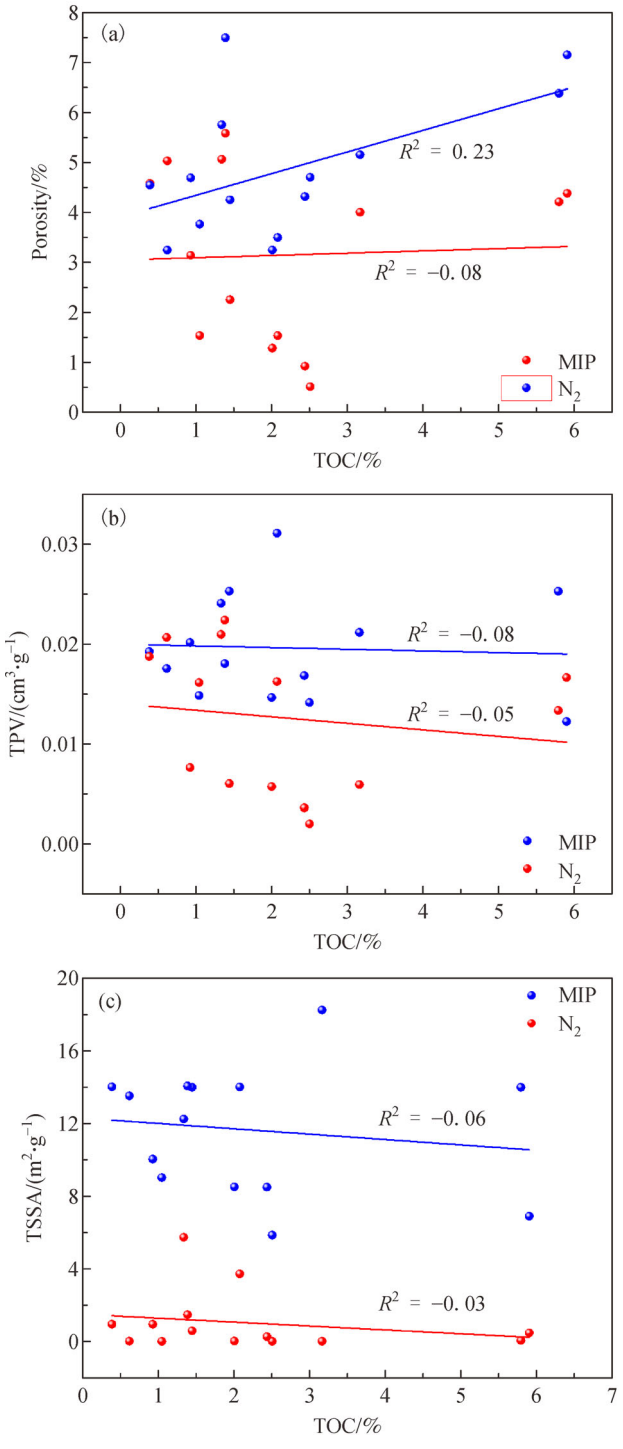

Fig. 15 The impact on pore structure of the shale from organic geochemical characteristics: (a) TOC vs porosity; (b) TOC vs TPV; (c) TOC vs TSSA; MIP: data obtained based on mercury injection experiment (MIP); N_2 adsorption: data obtained from the low temperature N_2 adsorption experiment.

produced, and the specific surface area and volume of the pores will increase. However, as the buried depth increases, mechanical compaction increases, and the pore size and pore space of shale decrease. Figure 16 illustrates the relationship between TOC content and fractal parameter D_1. Based on Fig. 16, the D_1 tends to decrease with TOC content increasing, indicating that with the increase in organic pores, the spatial complexity of pore surface decrease.

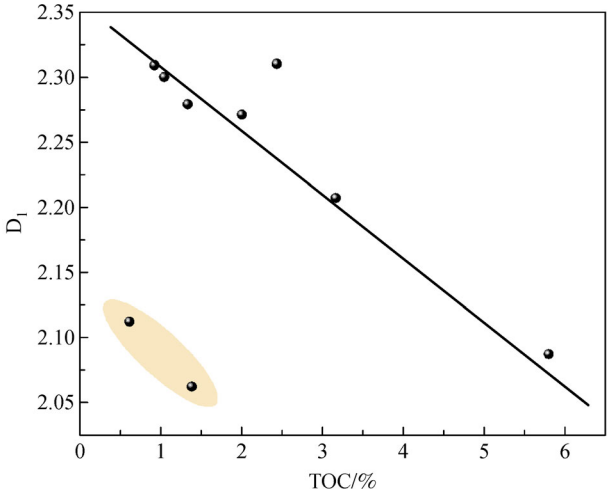

Fig. 16 The relationship between TOC content and fractal parameter D_1.

Kerogen releases a large amount of oil and gas during cracking and hydrocarbon expulsion (Jarvie et al., 2007; Bernard et al., 2012; Curtis et al., 2012). The number of organic nanopores increases with increasing maturity, especially in the gas generation stage (R_o = 0.7%–2.0%). Figure 17 shows the effect of shale maturity on total surface area which is obtained from the low temperature N_2 adsorption experiment (BET model). In general, the

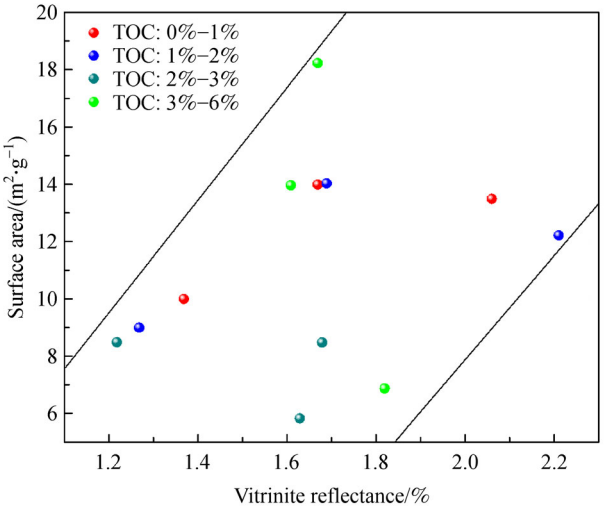

Fig. 17 The effect of vitrinite reflectance on surface area obtained from the low temperature N_2 adsorption experiment.

total surface area tends to increase with increasing vitrinite reflectance. This may be because there are more nanoscale pores generated in the maturation process. Besides, Fig. 18 shows the correlations of total volume (obtained from mercury injection experiment and low temperature N_2 adsorption experiment) and vitrinite reflectance. It is obvious that pore volume increase with the increase in vitrinite reflectance. Additionally, in shale samples with different TOC content, the evolution of pore surface area is different. During geological process, the clay minerals also change along with the organic matter. The changes in clay minerals can also affect the surface area in shale samples. And this makes the evolution of pore structure complex.

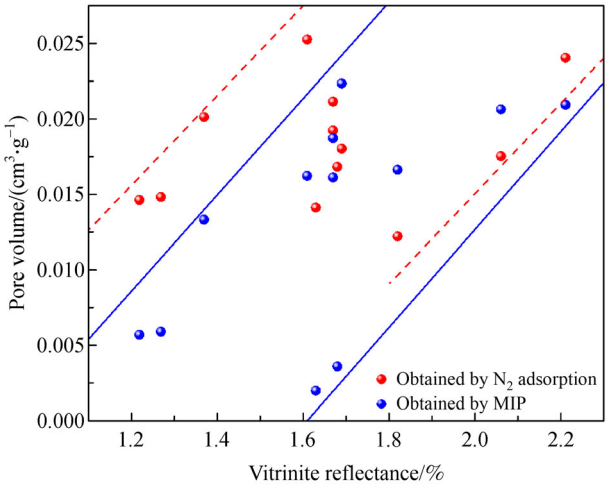

Fig. 18 The correlation between pore volume and vitrinite reflectance in shale samples.

5.3 The effect of clay minerals on pore structure

Inorganic pores in shale reservoirs are related to the mineral type, mineral abundance, and contact between minerals (Loucks et al., 2012). Due to the special sedimentary and diagenetic environment of continental shale reservoirs, the clay mineral content is generally higher than that of quartz and feldspar (Table 1). Although clay minerals occupy more than 50%, the organic matter also have significant effect on the pore structure. From Fig. 19, it can be seen that when the TOC content is 1%–2%, the surface area decreases with the kaolinite content. It means with the kaolinite changing to the illinite, more pores are generated. However, when TOC content is $< 1\%$, the surface area increase with increase kaolinite. In this case, kaolinite have greater effect on the pore surface area, and there are more pores in shale with higher kaolinite content. When TOC content is higher than 2%, the correlation between surface area and kaolinite content is weak, which means the kaolinite has weak effect on the pore structure.

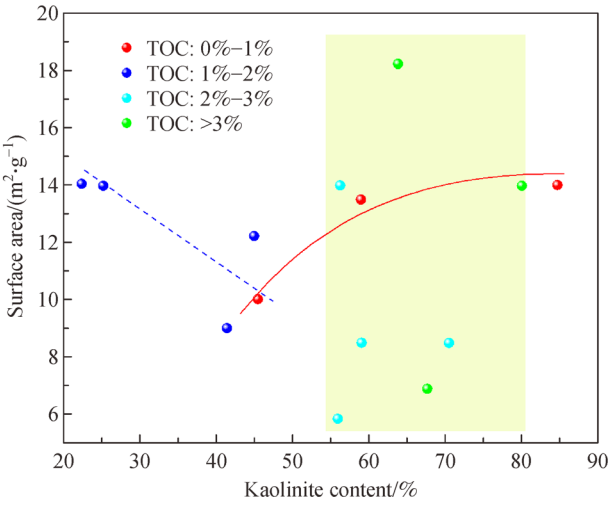

Fig. 19 The correlation between kaolinite content and surface area.

5.4 Comprehensive analysis of the evolution of pore structure

As shown by the SEM images, the pores are mainly formed by organic matter and clay minerals. In shale samples of Ningwu Basin, clay occupy 43.7% to 90% of the total minerals, and the clay minerals are mainly composed by kaolinite. The large amount of kaolinite minerals brings many pores in the kaolinite minerals. In addition, during the maturation process, many organic pores can be formed as the hydrocarbon are released from the shale kerogen. For the quartz, the pores can only be formed between the quartz particles. These pores are rare and usually in large scale.

Figure 20 presents the evolution of pore structure in organic shale with type III kerogen in Ningwu Basin. The depositional environment, evolution of inorganic matter and evolution of organic matter have great influence on the pore structure of shale (Li et al., 2019a). The composition of shale samples are controlled by deposition environment and the shale evolution. Based on our data, when the TOC content is lower than 1.4%, the clay content decreases linearly and the quartz content increases with an increase in TOC. In contrast, when the TOC content is higher than 1.4%, the clay content increases and the quartz content decreases with an increase in TOC (Fig. 18). After deposition, the organic matter and inorganic matter significantly changed during the late Hercynian and the early to middle Yanshan periods, as the pressure and temperature increasing significantly. The changes in mineral and organic composition would bring the changes in pores structure. As shown in Fig. 17, the fractal parameter D_1 tends to decrease with increasing the TOC content. In the geologic process, the temperature, pressure and geofluids would bring the changes in clay mineral type and organic structure. During the evolution, kaolinite tends

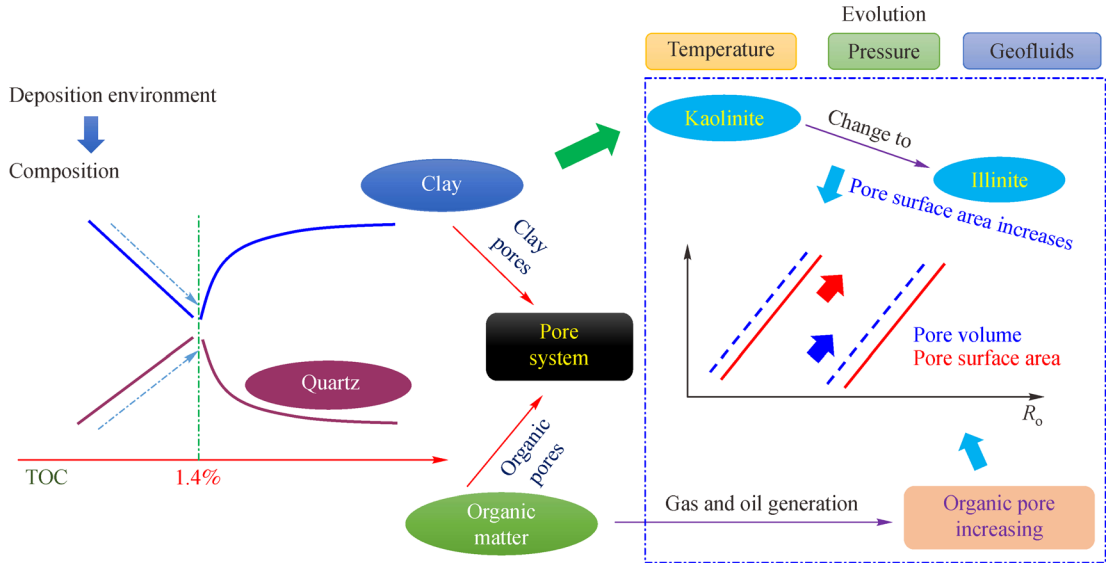

Fig. 20 Comprehensive analysis of pore structure in shale.

to turn the illite and as the same, the pore surface area increases. Besides, with the maturity of organic matter increasing, the pore volume and pore surface area both increase, which means the more organic pores are generated during the maturation process (Curtis et al., 2012; Xu et al., 2020). In addition, during the late Yanshan periods, strong compressive stress would also change the pore structure.

6 Conclusions

In the study, the pore characteristics and its evolution in shale with high kaolinite content and type III kerogen were investigated. Following conclusions can be drawn:

1) The N_2 adsorption results show that the shale adsorption curves of the shale samples are mianly types H3 and H4. Based on the FHH model, the N_2 adsorption method was used to calculate the fractal dimension of the pores. The parameter D_1 ranges from 2.062 to 2.310, with an average of 2.215, and D_2 ranges from 2.668 to 2.828, with an average of 2.756.

2) The depositional environment significantly affects the composition. For these shale samples, the kaolinite content decreases linearly with increasing the TOC content when the TOC is $< 1.4\%$. When TOC is $> 1.4\%$, the kaolinite content increases with TOC increment.

3) Based on the SEM images, high amount of organic pores and clay pores were found in shale samples with type III kerogen and high kaolinite content. There are also some inter-particle pores among pyrites and quartz particles.

4) During the maturation process, the kaolinite content decreases and illite content increases with increasing the vitrinite reflectance, indicating some kaolinite minerals change to illite. The pore volume and pore surface area both increase with increasing the vitrinite reflectance, and it may be because more organic pores and clay pores formed by in the illite were generated during the maturation process.

Acknowledgements This research is financial supported by National Natural Science Foundation of China (Grant No. 41872179).

References

Avnir D, Jaroniec M (1989). An isotherm equation for adsorption on fractal surfaces of heterogeneous porous materials. Langmuir, 5(6): 1431–1433

Bahadur J, Ruppert L F, Pipich V, Sakurovs R, Melnichenko Y B (2018). Porosity of the Marcellus Shale: a contrast matching small-angle neutron scattering study. Int J Coal Geol, 188: 156–164

Bernard S, Horsfield B, Schulz H M, Wirth R, Schreiber A, Sherwood N (2012). Geochemical evolution of organic-rich shales with increasing maturity: a STXM and TEM study of the Posidonia Shale (Lower Toarcian, northern Germany). Marine Petrol Geo, 31(1): 70–89

Brunauer S, Deming L S, Deming W E, Teller E (1940). On the theory of Van der Waal's adsorption of gases. J Am Chem Soc, 62(7): 1723–1732

Chen Y, Xu J, Wang P (2020). Shale gas potential in China: a production forecast of the Wufeng-Longmaxi Formation and implications for future development. Energ Polic, 147: 111868

Clarkson C R, Solano N R, Bustin R M, Bustin A M M, Chalmers G R L, He L, Melnichenko Y B, Radliński A P, Blach T P (2013). Pore structure characterization of North American shale gas reservoirs using USANS/SANS, gas adsorption, and mercury intrusion. Fuel, 103: 606–616

Curtis J B (2002). Fractured shale-gas systems. AAPG Bull, 86(11):

1921–1938

Curtis M E, Cardott B J, Sondergeld C H, Rai C S (2012). Development of organic porosity in the woodford shale with increasing thermal maturity. Int J Coal Geol, 103: 26–31

Feng Z, Dong D, Tian J, Qiu Z, Wu W, Zhang C (2018). Geochemical characteristics of Longmaxi Formation shale gas in the Weiyuan area, Sichuan Basin, China. J Petrol Sci Eng, 167: 538–548

Fu H, Wang X, Zhang L, Gao R, Li Z, Xu T, Zhu X, Xu W, Li Q (2015). Investigation of the factors that control the development of pore structure in lacustrine shale: a case study of block X in the Ordos Basin, China. J Nat Gas Sci Eng, 26: 1422–1432

Guo X (2019). Major factors controlling the shale gas accumulations in Wufeng-Longmaxi Formation of the Pingqiao Shale Gas Field in Fuling Area, Sichuan Basin, China. J Nat Gas Geosci, 4(3): 129–138

Hazra B, Wood D A, Kumar S, Saha S, Dutta S, Kumari P, Singh A K (2018). Fractal disposition, porosity characterization and relationships to thermal maturity for the Lower Permian Raniganj Basin shales, India. J Nat Gas Sci Eng, 59: 452–465

Jarvie D M, Hill R J, Ruble T E, Pollastro R M (2007). Unconventional shale-gas systems: the Mississippian Barnett Shale of north-central Texas as one model for thermogenic shale-gas assessment. AAPG Bull, 91(4): 475–499

Jiang F, Chen D, Wang Z, Xu Z, Chen J, Liu L, Huyan Y, Liu Y (2016). Pore characteristic analysis of a lacustrine shale: a case study in the Ordos Basin, NW China. Mar Pet Geol, 73: 554–571

Jiang P, Xu J (1989). Formation and evolution of the Ningwu Basin as a Mesozoic pull-apart basin. Chinese J Geo, 24(4): 314–322

Kanniah V, Wu P, Mandzy N, Grulke E A (2012). Fractal analysisasa complimentary technique for characterizing nanoparticle size distributions. Powder Technol, 226: 189–198

Katz B J, Arango I (2018). Organic porosity: a geochemist's view of the current state of understanding. Org Geochem, 123: 1–16

Kuang L, Dong D, He W, Wen S, Sun S, Li S, Qiu Z, Liao X, Li Y, Wu J, Zhang L, Shi Z, Guo W, Zhang S (2020). Geological characteristics and development potential of transitional shale gas in the east margin of the Ordos Basin, NW China. Petrol Explor Devel, 47(3): 471–482

Li J, Zhou S, Li Y, Ma Y, Yang Y, Li C (2016c). Effect of organic matter on pore structure of mature lacustrine organic-rich shale: a case study of the Triassic Yanchang shale, Ordos Basin, China. Fuel, 185: 421–431

Li Y, Tang D, Wu P, Niu X, Wang K, Qiao P, Wang Z (2016a). Continuous unconventional natural gas accumulations of Carboniferous-Permian coal-bearing strata in the Linxing area, northeastern Ordos Basin, China. J Nat Gas Sci Eng, 36: 314–327

Li Y, Wang Z, Gan Q, Niu X, Xu W (2019a). Paleoenvironmental conditions and organic matter accumulation in Upper Paleozoic organic-rich rocks in the east margin of the Ordos Basin, China. Fuel, 252: 172–187

Li Y, Yang J, Pan Z, Meng S, Wang K, Niu X (2019b). Unconventional natural gas accumulations in stacked deposits: a discussion of Upper Paleozoic coal-bearing strata in the east margin of the Ordos Basin, China. Acta Geol Sin (English Ed) , 93(1): 111–129

Li Y, Yang J, Pan Z, Tong W (2020). Nanoscale pore structure and mechanical property analysis of coal: an insight combining AFM and SEM images. Fuel, 260: 116352

Li Y, Zhang C, Tang D, Gan Q, Niu X, Wang K, Shen R (2017). Coal pore size distributions controlled by the coalification process: an experimental study of coals from the Junggar, Ordos, and Qinshui basins in China. Fuel, 206: 352–363

Li Z, Oyediran I A, Huang R, Hu F, Du T, Hu R, Li X (2016b). Study on pore structure characteristics of marine and continental shale in China. J Nat Gas Sci Eng, 33: 143–152

Li Z, Shen X, Qi Z, Hu R (2018). Study on the pore structure and fractal characteristics of marine and continental shale based on mercury porosimetry, N_2 adsorption and NMR methods. J Nat Gas Sci Eng, 53: 12–21

Liu G, Huang Z, Chen F, Jiang Z, Gao X, Li T, Chen L, Xia L, Han W (2016). Reservoir characterization of Chang 7 member shale: a case study of lacustrine shale in the Yanchang Formation, Ordos Basin, China. J Nat Gas Sci Eng, 34: 458–471

Liu K, Ostadhassan M, Sun L, Zou J, Yuan Y, Gentzis T, Zhang Y, Carvajal-Ortiz H, RezaeeR(2019). A comprehensive pore structure study of the Bakken Shale with SANS, N_2 adsorption and mercury intrusion. Fuel, 245: 274–285

Liu W, Wu J, Jiang H, Zhou Z, Luo C, Wu W, Li X, Liu S, Deng B (2021). Cenozoic exhumation and shale-gas enrichment of the Wufeng-Longmaxi formation in the southern Sichuan Basin, western China. Mar Pet Geol, 125: 104865

Liu X, Xiong J, Liang L (2015). Investigation of pore structure and fractal characteristics of organic-rich Yanchang formation shale in central China by nitrogen adsorption/desorption analysis. J Nat Gas Sci Eng, 22(7): 62–72

Loucks R G, Reed R M, Ruppel S C, Hammes U (2012). Spectrum of pore types and networks in mudrocks and a descriptive classification for matrix-related mudrock pores. AAPG Bull, 96(6): 1071–1098

Nie H, Li D, Liu G, Lu Z, Hu W, Wang R, Zhang G (2020). An overview of the geology and production of the Fuling shale gas field, Sichuan Basin, China. Energy Geoscience, 1(3–4): 147–164

Pan Y, Hui D, Luo P, Zhang Y, Zhang L, Sun L (2018). Influences of subcritical and supercritical CO_2 treatment on the pore structure characteristics of marine and terrestrial shales. J CO_2 Utilization, 28: 152–67

Qin L, Li S, Zhai C, Lin H, Zhao P, Shi Y, Bai Y (2020). Changes in the pore structure of lignite after repeated cycles of liquid nitrogen freezing as determined by nitrogen adsorption and mercury intrusion. Fuel, 267: 117214

Sanyal D, Ramachandrarao P, Gupta O P A (2006). Fractal description of transport phenomena in dendritic porous network. Chem Eng Sci, 61(2): 307–315

Shi M, Yu B, Xue Z, Wu J, Yuan Y (2015). Pore characteristics of organic-rich shaleswith high thermal maturity: a case study of the Longmaxi gas shale reservoirs from well Yuye-1 in southeastern Chongqing, China. J Nat Gas Sci Eng, 26: 948–959

Slatt R M, O'Brien N R (2011). Pore types in the Barnett and Woodford gas shales: contribution to understanding gas storage and migration pathways in fine-grained rocks. AAPG Bull, 95(12): 2017–2030

Sun C, Tang S, Zhang S, Wei J, Hou Y, Zhang T (2017). Nanopore characteristics of Late Paleozoic transitional facies coal-bearing shale in Ningwu Basin, China investigated by nuclear magnetic resonance and low-pressure nitrogen adsorption. J Nanosci Nanotechnol, 17(9): 6433–6444

Wang Q, Chen X, Jha A N, Rogers H (2014a). Natural gas from shale

formation- the evolution, evidences and challenges of shale gas revolution in United States. Renew Sustain Energy Rev, 30(2): 1–28

Wang X, Gao S, Gao C (2014b). Geological features of Mesozoic lacustrine shale gas in south of Ordos Basin, NW China. Pet Explor Dev, 41(3): 326–337

Wang X, Zhu Y, Song Y, Jonathan P (2020). Structure and partial ordering of terrestrial kerogen: insight from high-resolution transmission electron microscopy. Fuel, 281: 118759

Wang Y, Wang L, Wang J, Jiang Z, Jin C, Wang Y (2018). Characterization of organic matter pores in typical marine and terrestrial shales, China. J Nat Gas Sci Eng, 49: 56–65

Wang Y, Wang L, Wang J, Jiang Z, Wang C, Fu Y, Song F, Wang Y, Liu D, Jin C (2019). Multiscale characterization of three-dimensional pore structures in a shale gas reservoir: a case study of the Longmaxi shale in Sichuan Basin, China. J Nat Gas Sci Eng, 66: 207–216

Xiong F, Jiang Z, Li P, Wang X, Bi H, Li Y, Wang Z, Amooie M A, Soltanian M R, Moortgat J(2017). Pore structure of transitional shales in the Ordos Basin, NW China: effects of composition on gas storage capacity. Fuel, 206: 504–515

Xu Q, Liu B, Ma Y, Song X, Wang Y, Chen Z (2017). Geological and geochemical characterization of lacustrine shale: a case study of the Jurassic Da'anzhai member shale in the central Sichuan Basin, southwest China. J Nat Gas Sci Eng, 47: 124–139

Xu Q, Xu F, Jiang B, Zhao Y, Zhao X, Ding R, Wang J (2018). Geology and transitional shale gas resource potentials in the Ningwu Basin, China. Energy Explor & Exploit, 36(6): 1482–1497

Yang F, Ning Z, Liu H (2014). Fractal characteristics of shales from a shale gas reservoir in the Sichuan Basin, China. Fuel, 115: 378–384

Yang F, Ning Z, Wang Q, Zhang R, Krooss B M (2016a). Pore structure characteristics of lower Silurian shales in the southern Sichuan Basin, China: insights to pore development and gas storage mechanism. Int J Coal Geol, 156: 12–24

Yang Y, Zhang W, Gao Y, Wan Y, Su Y, An S, Sun H, Zhang L, Zhao J, Liu L (2016b). Influence of stress sensitivity on microscopic pore structure and fluid flow in porous media. J Nat Gas Sci Eng, 36 (Part A): 20–31

Yang R, He S, Yi J, Hu Q (2016c). Nano-scale pore structure and fractal dimension of organic-rich Wufeng-Longmaxi shale from Jiaoshiba area, Sichuan Basin: investigations using FE-SEM, gas adsorption and helium pycnometry. Mar Pet Geol, 70: 27–45

Yuan Y, Rezaee R (2019). Fractal analysis of the pore structure for clay bound water and potential gas storage in shales based on NMR and N_2 gas adsorption. J Petrol Sci Eng, 177: 756–765

Zhang B X, Fu X H, Shen Y L, Zhang Q H, Deng Z (2021). Mineral composition and its control on nanopores of marine-continental transitional shale from the Ningwu Basin, North China. J Nanosci Nanotechnol, 21(1): 168–180

Zhang J, Li X, Xie Z, Li J, Zhang X, Sun K, Wang F (2018). Characterization of microscopic pore types and structures in marine shale: examples from the Upper Permian Dalong Formation, Northern Sichuan Basin, South China. J Nat Gas Sci Eng, 59: 326–342

Zhang M, Fu X, Zhang Q, Cheng W (2019). Research on the organic geochemical and mineral composition properties and its influence on pore structure of coal-measure shales in Yushe-Wuxiang Block, South Central Qinshui Basin, China. J Petrol Sci Eng, 173: 1065–1079

Zhou J, Yang K, Tian S, Zhou L, Xian X, Jiang Y, Liu M, Cai J (2020). CO_2-water-shale interaction induced shale microstructural alteration. Fuel, 263: 116642

Zhou L, Kang Z (2016). Fractal characterization of pores in shales using NMR: a case study from the Lower Cambrian Niutitang Formation in the Middle Yangtze Platform, Southwest China. J Nat Gas Sci Eng, 35: 860–872